

# Probabilistic Absolute Position Sensor based on Objective Laser Speckles

Rene Paris, Martin Melik-Merkumians, Georg Schitter  
Automation and Control Institute  
Vienna University of Technology  
Gußhausstraße 27-29, A-1040 Vienna, Austria  
{paris, melik-merkumians, schitter}@acin.tuwien.ac.at

**Abstract**—This contribution presents a vision-based probabilistic absolute position sensor which is able to operate on spacious technical surfaces without modification of the surface. Instead of using artificial surface markings, the surface structure itself is used to generate objective laser speckle patterns, which are observable on most technical surfaces. This allows extraction of features on surfaces, which might be too smooth for image processing under white light observation. In addition, the uniqueness of the individually observed laser speckle patterns enables a determination of the absolute position even after a sudden power loss of the sensor system. Experiments confirm the applicability of such objective laser speckle patterns within a feature based probabilistic framework on a smooth stainless steel rod and compare the results to images taken under white light illumination. The proposed sensor system successfully recovers from unknown initial states and measures the position with a peak to peak error of  $22.1\ \mu\text{m}$  and an RMS error of  $5.6\ \mu\text{m}$  over a measurement range of 100 mm.

## I. INTRODUCTION

Measuring the absolute position of a flat spacious technical surface is a challenging task but at the same time desirable for various types of applications, such as position measurement and control of linear actuators or machine elements.

The importance of this task is reflected by the variety of available sensor principles, such as optical triangulation sensors, laser interferometers, magnetostrictive (MS) sensors, linear variable differential transformers (LVDTs), high-frequency resonant contactless inductive (HFRCI) position sensors, and magnetic as well as optical absolute encoders, which are reported in [1], [2], [3].

All these measurement principles are contactless, which is a general demand for a long service live. An often overlooked point is that also the moving surface must be designed for a long service, both in terms of guiding bearings and material for specific mechanical properties. In such cases modifying the surface finish or the material composition of the measurement target is unacceptable.

Another complicating factor is that the abutting face of a spacious surface is often not accessible. This cancels out sensors which can only measure the out-of-plane component, such as triangulation sensors and laser interferometers [1]. Magnetic encoders, LVDTs, and MS sensors [2] cannot be used, as they need magnetic marks or a magnetic permeable

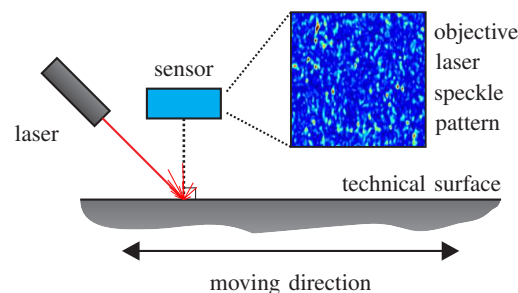


Fig. 1: An optical sensor mounted in parallel to an untreated surface of an arbitrary technical surface. The coherent light of the laser allows observation of Objective Laser Speckle Pattern with high contrast from technically smooth surfaces.

core. This also holds true for planar HFRCI position sensors [3], as they need a passive LC resonator attached to the moving target.

Linear incremental optical encoders are commonly used as they offer excellent linearity and some types achieve a resolution better than  $0.1\ \mu\text{m}$  over a measurement range of several meters [3]. As a consequence, a lot of effort has been taken to convert relative optical encoders into absolute encoders, such as by means of phase-encoded binary codes [4] or etching a pseudo random pattern into the glass scale [5]. A more general approach is based on Digital Image Correlation (DIC), which is widely used to measure surface deformation of materials and structures in experimental solid mechanics [6]. In [7] an absolute sensor is presented, which uses DIC in combination with optimized two-dimensional reference marks, based on a specially coded non-periodic microstructure. Note that the reference marks are artificially produced pieces of silicon substrate coated with chromium, which also cannot be used in the given case.

None of the so far presented techniques operate without modification of the surface, especially if the surface roughness is rather low and does not exhibit distinguishable intensity distributions if imaged under regular illumination. This lack of features on smooth surfaces has been successfully tackled in [8] by means of Laser Speckle Patterns (LSPs) generated by

coherent laser illumination, showing an approach towards an absolute scale of a machine tool. LSPs are an interferometric phenomenon caused by coherent light scattered back by a surface with a roughness on the order of the wavelength of the illumination or above [9]. Due to their nature, LSPs are observable on most technical surfaces and show a high contrast. As the surface structure can be regarded as randomly distributed, the observed patterns can be used as unique intensity distributions which supersede artificial markers.

Still, the database method generates a huge image database of LSPs which is directly proportional to memory consumption. Memory consumption can be reduced by decreasing the grid density and interpolation between grid points based on the (de-)correlation function of LSPs [10]. To a certain extent [11] improve the concept by a dual wavelength approach, but as the authors point out LSPs are sensitive to environmental disturbances and any contamination of the sample. As a consequence a purely correlation based approach is difficult to implement. In addition, for long stroke applications the memory consumption is still an open issue.

Recently a vision-based probabilistic absolute position sensor [12] has been presented. The proposed sensor system uses a Particle Filter (PF) in conjunction with features extracted from regular camera images to estimate its position within a once-only learned global feature map instead of an image database.

Although the concept is memory efficient, the system uses white light illumination and, as such struggles with smooth surfaces as contrast and feature density degrades. The following contribution extends this concept by usage of features extracted from Objective Laser Speckle Patterns (Fig. 1) and takes advantage of the intrinsic robustness of PFs against erroneous observations, such as fluctuating speckle grains. The results are compared to a system operating under white light illumination.

This contribution is organized as follows. In Section II a short introduction on LSP and probabilistic localization based on a PF is given. Section III presents the proposed approach, followed by the implementation in Section IV, which is itself divided into the laboratory setup, feature detection, differences in the illumination strategies for feature detection, and generation of the global feature map. Results are presented in Section V, discussing statistical independence of the database images, the position accuracy of the compared systems, and the state recovery behavior in detail.

## II. THEORETICAL BACKGROUND

The following section gives an introduction on LSPs, which are the basis for the image processing stage of the proposed sensor. In addition, probabilistic localization based on PFs is briefly discussed, which forms the algorithmic core of the sensor.

### A. Laser Speckle Patterns

LSPs are an interferometric phenomenon, arising when coherent light is being scattered by an optically rough surface [9]. The following contribution relies purely on the special case of Objective Laser Speckle Pattern (OLSP), which can

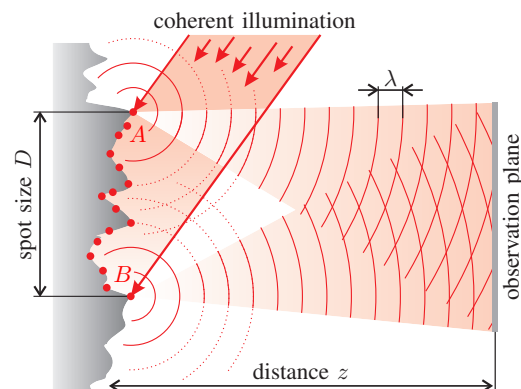


Fig. 2: Formation of Objective Laser Speckle Patterns: Every surface point within the illuminated spot, such as  $A$  and  $B$ , scatters the incoming coherent light. The emerging wavelets with wavelength  $\lambda$  but different phase (different optical path length) interfere at the observation plane.

be observed if the scattered coherent light is imaged at an observation plane without any lens in the imaging path (Fig. 2), which is also referred to as free-space propagation. As a consequence, the whole illuminated area contributes to each point of the observation plane. Note that Subjective Laser Speckle Patterns, which are observed using an imaging system, is not further discussed here.

According to the *Huygens-Fresnel* principle every refracting surface point, such as  $A$  and  $B$  in Fig. 2, can be regarded as source for a new wavelet. Since no lens is used, the wavelets propagate freely towards the observation plane where they interfere. The random and unknown height variations of the surface lead to a random optical path lengths for each wavelet at the observation plane, which results in locally distributed occurrences of constructive as well as destructive interferences. Maximum contrast is observed, if the optical path difference between the individual wavelets and the observation point is on the order of a single wavelength or higher. This leads to the typical OLSPs, covering the whole observation plane with high contrast. OLSPs do not suffer from lens aberrations [13] and, can be used for very local measurement at smallest specimen and surface areas [14] if the illumination area is adjusted to the measurement area.

Speckles can be observed at most technical surfaces, such as non-polished metallic surfaces, and show a high contrast (cf. Fig. 1), which makes pre-treatment of the surface, such as artificial markers, typically unnecessary. The proposed sensor relies on OLSPs as they allow a very compact overall design without a costly lens-system. The resulting compactness of the system is bought by an increased susceptibility to ambient light, which is deliberately accepted and taken into account by proper shielding.

Properties of speckle fields are typically expressed by statistical means in terms of correlation functions of their complex amplitude or intensity [9]. The average in-plane speckle size,

derived from the auto-correlation of a random speckle field, is given by

$$d = 1.22 \frac{\lambda z}{D} \quad (1)$$

for OLSPs, where  $\lambda$  is the wavelength of the illumination,  $z$  is the distance between surface and observation plane, and  $D$  is the diameter of the illumination spot. Note that the speckle size only depends on geometrical relations and not on the surface roughness. Under the assumption of a purely in-plane movement without strain, OLSPs can be utilized to determine translational movement at high precision using cross-correlation of speckle fields [8], [10], [15]. The digital resolution depends on the signal processing algorithm and is typically on the order of  $\frac{1}{10}$  to  $\frac{1}{20}$  of the pixel size [16].

### B. Probabilistic Localization

Similar to vision-based localization, sensor readings are not taken from the whole image, but from observation of known landmarks stored in a global map [17]. The actual position within the map is eventually estimated using a PF. In the following the steps necessary for performing this probabilistic localization is given, following to a large extend [18].

Let the true position of the sensor be described by the state vector  $\mathbf{x}_t = (x \ y)^T$ , which refers to the global coordinates at time  $t$ . As depicted in Fig. 1 the actuation direction is assumed to be along the  $x$  axis.

Under the *Markov assumption*, stating that  $\mathbf{x}_t$  is complete and the best predictor of the future, it only depends on its previous state  $\mathbf{x}_{t-1}$  and the actual control inputs  $\mathbf{u}_t$ . This dependence is described by the *state transition probability*  $p(\mathbf{x}_t | \mathbf{x}_{t-1}, \mathbf{u}_t)$ . Observations  $\mathbf{z}_t$  of the sensor are modeled by the *measurement probability*  $p(\mathbf{z}_t | \mathbf{x}_t, \mathbf{m})$ , taking the actual state and a global map  $\mathbf{m}$  into account.

The *belief* is defined by the conditional probability  $bel(\mathbf{x}_t) = p(\mathbf{x}_t | \mathbf{z}_t, \mathbf{u}_t)$  and reflects the knowledge of the sensor about the state of the environment. A recursive Bayes filter estimates  $bel(\mathbf{x}_t)$  from  $bel(\mathbf{x}_{t-1})$  by a *prediction* and an *update* step, incorporating  $\mathbf{u}_t$  and  $\mathbf{z}_t$ , respectively. The most prominent possibility to perform recursive Bayes localization is by means of the well-known Kalman filter [19].

The sensor readings  $\mathbf{z}_t$  emerge from the observation of known landmarks stored in a global map  $\mathbf{m}$ . The correspondence between observations and individual landmarks is typically established by the maximum likelihood of individual landmark descriptors, meaning that landmarks should be as unique as possible to prevent erroneous assignment. This data association problem can be catastrophic for Kalman filter based localization [18] and is one of the reasons for alternative approaches, such as PFs.

PFs estimate the actual state by a set of random state samples. This random set of samples, or particles, is denoted by  $\mathbf{X}_t := \mathbf{x}_t^{[1]}, \mathbf{x}_t^{[2]}, \dots, \mathbf{x}_t^{[N]}$ , with  $N$  being the number of particles used. The key idea is to represent the belief  $bel(\mathbf{x}_t)$ , also called Bayes filter posterior, by a particle density which has the same distribution as the belief itself. As  $N \rightarrow \infty$  the likelihood for the state hypothesis included in  $\mathbf{X}_t$  goes asymptotically towards the true posterior. A finite particle

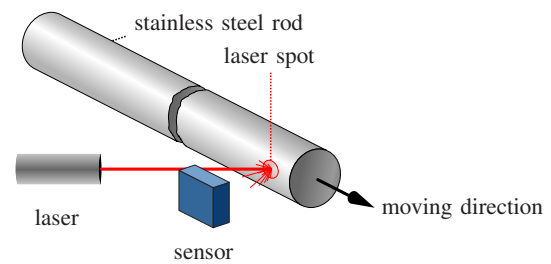


Fig. 3: Test case for the proposed system, using a stainless steel rod with a low surface roughness, observed under laser illumination.

count leads to a different distribution but in practice this difference can be neglected as long as  $N$  is large enough ( $N \geq 100$ ) [18].

PFs recursively estimate the posterior  $bel(\mathbf{x}_t)$  from  $bel(\mathbf{x}_{t-1})$ , meaning they construct  $\mathbf{X}_t$  from the random set  $\mathbf{X}_{t-1}$ . The algorithm consists of three steps:

- 1) *Prediction step*: Generate a state hypothesis  $\mathbf{x}_t^{[n]}$  for each individual particle  $n$  based on its former state  $\mathbf{x}_{t-1}^{[n]}$  and the control vector  $\mathbf{u}_t$  by sampling from the state transition probability  $p(\mathbf{x}_t | \mathbf{x}_{t-1}, \mathbf{u}_t)$ .
- 2) *Update step*: Weight each particle by incorporating the measurement vector  $\mathbf{z}_t$  by means of the measurement probability  $w_t^{[n]} = p(\mathbf{z}_t | \mathbf{x}_t^{[n]}, \mathbf{m})$ , where the scalar  $w_t$  is called *importance weight*.
- 3) *Importance sampling*: Approximating  $bel(\mathbf{x}_t)$  by drawing  $N$  particles with replacement from the actual set based on their weight.

An advantage of PFs over single hypothesis recursive Bayes filter is their ability to cope with erroneous data associations. Each particle evaluates observations only with respect to itself. If an observation is now assigned to the wrong landmark, only the state of the actual particle will be altered. This will lead to a decreased importance factor for the altered particle and as a consequence this particle is less likely to be resampled during the importance sampling step and will "die out".

### III. PROPOSED APPROACH

The proposed sensor system closely follows [12], but with the main difference that the target is now an arbitrary technical surface observed under laser illumination (Fig. 3). The sensor extracts features of interest from the sensor image before estimating the position using a PF.

In order to show the weaknesses and strengths of the proposed sensor, two illumination strategies are used. One works with images of the surface taken with LED illumination (white light illumination), the other does feature extraction based on Objective Laser Speckle Pattern using laser illumination. For proper comparison of the results, a test surface is selected, which allows extraction of features under both illumination scenarios, but smooth enough to emphasize the limits of white light illumination. The test case is a stainless steel rod

whose curvature additionally highlights the strength of a very localized measurement technique over conventional camera based processing (c.f. Section IV-C).

The extracted features are then used to estimate the actual state, reflecting the actual position of the rod. The *state hypothesis* within the *prediction step* is modeled by  $\mathbf{x}_t = \mathbf{x}_{t-1} + \mathbf{u} + \epsilon$ , where the control input  $\mathbf{u}$  is generated from the actual frame-to-frame displacement, and the random term  $\epsilon$  is a random displacement based on the variance over all displacements during map generation (see Section IV-D).

To enable absolute position measurement, a once-only initial scan of the surface is executed, the coordinates of selected features are extracted, and a global map is generated. During operation, the coordinates of all visible features  $\mathbf{z}$  within the map  $\mathbf{m}$  are taken into account within the *update step*. Feature coordinates extracted from the live image are set into a 1:1 relation with respect to the global map by a nearest neighbor search [20]. Measurement noise is expected to stem from fluctuations of the measured coordinates caused by the image sampling, blind spots on the sampling pixels itself, but also due to pattern decorrelation under laser illumination. For calculation of the normalized *importance weight*  $w_t^{[n]}$  the measurement noise is assumed to be normally distributed. This might not reflect the exact noise generated by the feature detector, but is robust enough to cope with small modeling errors [18]. It also allows to use the Mahalanobis distance [21] as weighting base, which enables a direct incorporation of the covariance extracted during map generation. Since no rotational movement is expected (see Section IV),  $x$  and  $y$  variances are assumed to be independent. This finally leads to a diagonal covariance matrix which further reduces the calculation to the normalized Euclidean distance

$$d(\mathbf{m}, \mathbf{z}_t^{[n]}) = \sqrt{\frac{(m_x - z_{t,x}^{[n]})^2}{s_x^2} + \frac{(m_y - z_{t,y}^{[n]})^2}{s_y^2}}, \quad (2)$$

where  $\mathbf{z}_t^{[n]} = (z_{t,x}^{[n]} \ z_{t,y}^{[n]})^T$  are the coordinates of the current observations with respect to the particle  $n$ ,  $\mathbf{m} = (m_x \ m_y)^T$  are the matched map coordinates, and  $s_x$  and  $s_y$  are the standard deviations of these coordinates. The distance is evaluated for each particle and leads after normalization to the importance weights  $w_t^{[n]}$ .

Finally the sensor position  $\mathbf{x}_{est}$  is estimated by taking the weighted average with respect to each individual state hypotheses  $\mathbf{x}_t^{[n]}$  before resampling by

$$\mathbf{x}_{est} = \sum_{n=1}^N w_t^{[n]} \mathbf{x}_t^{[n]}. \quad (3)$$

#### IV. IMPLEMENTATION

Two implementations of the vision-based probabilistic absolute position sensor [12] are compared to each other. The first uses incoherent illumination by white light and a microscope objective. The second utilizes images taken from observation of OLSPs, which are generated by a coherent laser source. Both implementations operate on the same steel rod whose surface is selected to be still resolvable by the imaging system.

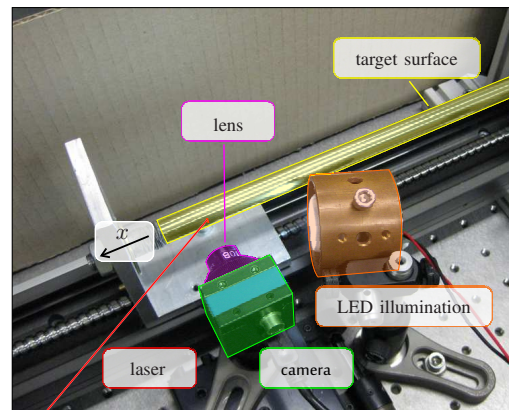


Fig. 4: Setup with cylindrical rod (target surface) imaged by the camera and actuated along its  $x$  axis. White light experiments are conducted with LED illumination and a lens. For observation of OLSPs the laser illumination was used and the lens was removed.

#### A. Laboratory setup

The laboratory setup (Fig. 4) consists of a camera mounted in parallel to a moveable target surface. The surface under test is a guided stainless steel rod, which is fixed against rotation and attached to an electric slide (EGSP-33-500-6P, Festo AG, Esslingen, Germany). The slide is based on a spindle drive with shaft joint actuated by a stepper motor (EMMS-ST-57-S-SE-G2, Festo AG, Esslingen, Germany), offering a repeatability of  $\pm 10 \mu\text{m}$ . The true position of the cylindrical rod is indirectly measured by the internal optical encoder of the stepper motor.

For the *white light experiments* a lens with a focal length of 12 mm and a magnification of 0.5 is used, resulting in a field of view of approximately  $10 \times 6.5 \text{ mm}$ . Illumination is done by diffuse white light using white LEDs and a diffuser.

For the experiments using *OLSPs*, the lens is removed and the illumination is changed to a linear polarized HeNe-laser (JDSU 1108P, Edmund Optics Inc., Barrington, USA) with a wavelength of  $\lambda = 632.8 \text{ nm}$ , an output power of 0.5 mW, and a beam diameter of 0.48 mm. The camera (DMK22BUC03, The Imaging Source Europe GmbH, Bremen, Germany) has an 8 bit gray scale CMOS sensor (MT9V024, Micron Technology Inc., Boise, Idaho, USA) with a maximum resolution of  $744 \times 480$  pixel at 76 fps and a square pixel pitch of  $6 \mu\text{m}$ . Exposure and gain values of the camera are fixed and adjusted manually for maximum contrast individuality for white light and laser illumination, respectively. For both illumination scenarios the gamma correction value is set to 0.83.

The setup is shielded from ambient light by a cardboard box. For the white light experiments this prevents random intensity fluctuations. In the case of OLSP observation, where no lens system is used and the sensor is directly exposed to ambient light, shielding is necessary to prevent sensor saturation. In

addition, precaution have been taken to absorb the majority of the reflected laser light by black masking tape. Otherwise information from the stationary shield would be mixed into the laser speckle field leading to erroneous speed calculations.

### B. Feature detection

Feature detection for PF based systems is a tradeoff between feature detection complexity and number of required particles. The less distinguishable features there are, the more particles are needed to cope with additional erroneous data associations. To guarantee a certain uniqueness of features, more complex detectors are used, which comes again at the price of increased computational effort [22]. For good performance, feature detection needs to be adapted for the task given.

For feature detection a scale-normalized Laplace of Gaussian (LoG) operator is used, which has been shown to be a reasonable choice to discover the intrinsic scale of spatially extended features, also called Binary Large Objects (BLOBs), in an image [23]. The Laplacian is a second order differential operator and the magnitude of its response has its maximum at the center of a BLOB, provided the scale of the Laplacian matches the scale of the BLOB. For increased robustness with respect to the second derivative the image is smoothed by the Gaussian part of the kernel. The size of a BLOB is detected by convolution of the image with Laplacians of different size and detection of the maximum absolute response. This scheme is executed on several image scales.

For surfaces with similar surface structure the size of the features can be estimated in advance. As a consequence the number of kernels for detection of different sizes and scales can be reduced to a minimum. Note that calculation of the sub-pixel position of the detected features can be omitted under the assumption that quantization errors occur statistically independent. As long as enough statistically independent features are visible at the same time, errors are averaged out by the PF itself. This expected quantization noise can be covered by increasing the standard deviation used in the Gaussian measurement model.

Since the sensor has a fixed sensor-to-surface orientation, rotational invariance can be ignored completely. In addition, the distance between sensor and surface can be regarded as constant, meaning that individual features need not to be detected at different scales. Nevertheless, under white light illumination surfaces naturally exhibit features which differ in size and shape. Note that speckles do not scale as one would assume normally for white light images, which will be discussed in the next section.

Summarizing, a BLOB detection stage based on the LoG operator applied to different scales of the image may be sufficient for robust detection of features, as demonstrated in [12]. For the actual implementation only the coordinates extracted by the LoG detector are used. This increases the performance, but does not allow for differentiation of individual features. For increased robustness, feature descriptors such as the commonly known Scale Invariant Feature Transform (SIFT) descriptor [24] can be extracted at the detected coordinates and additionally matched.

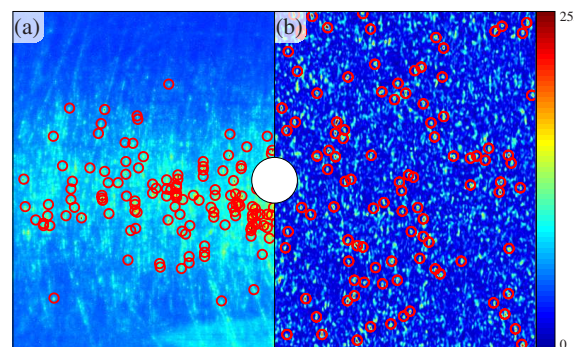


Fig. 5: Target surface imaged at the same position using (a) white light illumination and (b) laser illumination. The laser speckles show better contrast and a uniform distribution of detected features (red circles). The laser spot is sketched by the white circle in the middle.

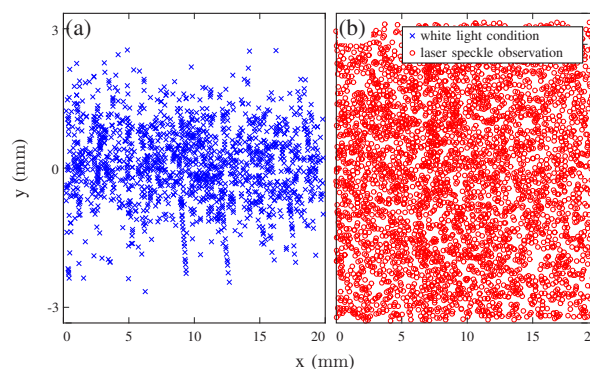


Fig. 6: Section of the global map generated (a) from white light illumination and (b) from observation of Objective Laser Speckle Patterns.

### C. White Light vs. Laser Illumination

This section discusses the differences between the two illumination strategies discussed earlier. For comparison, Fig. 5 shows an image of the cylindrical rod taken with white light (Fig. 5a) and laser illumination (Fig. 5b). Detected features are depicted by their positions with red circles. The white circle in the center of Fig. 5 sketches the size of the laser spot, which is only a fraction of the visible area used for the white light experiments.

Under white light illumination the curvature of the cylindrical target is clearly visible. As a consequence, features within the center are favored over those at the top and bottom. In addition, the position of the light source causes an intensity gradient from left to right further shaping the distribution of the detected features. Even if exposure is adjusted for best usage of the dynamic range of the camera, the overall contrast measured by standard deviation over mean intensity is only

0.30. Note that in general contrast degrades with decreasing surface roughness.

In the case of laser illumination OLSPs are observed, which are an interference pattern visible on the whole observation plane with high contrast. Note that it is not the shape of the surface which is being observed, which emphasizes the strength of the proposed approach over regular illumination. Fig. 5b shows that the detected features are uniformly distributed over the whole image, which has a contrast of 0.65.

For both implementations, the feature detector is adjusted individually. Under white light conditions, the size of detectable features as well as rejection ratio are adjusted manually to guarantee a dense map without too many occlusions at the center region. Under laser illumination the observed feature size and density is defined by the average size of the speckle grains  $d$ , which is given by the wavelength  $\lambda$ , the beam diameter  $D$ , and the sensor to surface distance  $z$  (see Equation (1)). The speckle size is chosen to be approximately 10 pixel, which is achieved by setting  $z = 40$  mm and without changing the beam diameter. This allows to detect a dense feature distribution, but is big enough to suppress negative effects of blind areas of the individual pixels. Note that the average size of the speckle grains stays the same independent of the actual position. As a consequence the size of the LoG kernel is set to a single matching value which increases the speed of the detector stage.

#### D. Global feature map

The state is estimated within a global feature map, which is generated once-only before the experiments in an independent scan for each illumination strategy. Due to the expected decorrelation of the OLSP the target is scanned with a step size of  $50 \mu\text{m}$ . For comparison the same step size has been taken for the white light experiment. Second, the scanned images are processed by the feature detector in order to extract the local  $x$  and  $y$  coordinates of each feature of interest.

To generate a global coordinate system, the local coordinates are corrected by a displacement with respect to the first image. The displacement is measured with a sub-pixel accuracy of 0.1 pixel by cross-correlation peak detection between consecutive images, as described in [15]. The corrected coordinates are stitched by averaging nearest neighbors within close proximity. The standard deviation for each merged coordinate is stored individually. Outliers are filtered by removing coordinates with high standard deviation. This filters unstable features, mainly caused by the decorrelation of the speckle pattern. A section of the resulting maps is shown in Fig. 6 for (a) white light and (b) laser illumination, clearly showing the differences in the coverage within the field of view.

The generated maps consists of 13 291 coordinates for white light and 40 194 coordinates for laser illumination. If stored as single precision floating point numbers and taking the stored standard deviations into account, the maps require only a memory of about 207 kB and 628 kB, respectively

For comparison, it is assumed that images are taken only every  $10^{\text{th}}$  increment of the desired resolution, as demonstrated earlier in [10] or [12]. This results in a step size of 1 mm or 101 images at full resolution, leading to a memory consumption of

35 224 kB. Compared to the proposed system, this is more than 169 times higher for white light illumination and still 56 times for observation of OLSP.

## V. RESULTS

In the following, the performance of the two implementations, one with white light and the other with laser illumination, are compared to each other. For all experiments, the ground truth is taken from the internal position sensor of the electric slide. Dynamic effects are prevented by testing under quasi-static conditions, meaning that the cylindrical rod is hold in position during image acquisition.

### A. Statistical Independence

To verify statistical independence of the recorded images, as necessary for an absolute position sensor, image resemblance is tested in the first experiment. Images of the target are recorded every  $50 \mu\text{m}$  over the whole stroke of 100 mm. This set is correlated to an additional set of 21 images, recorded every 5 mm. The normalized cross-correlation values for each comparison are shown in Fig. 7a for white light and Fig. 7b for laser illumination. Both implementations show significant peaks at the correct positions. Two major differences can be seen.

First, in contrast to the images recorded with white light, those recorded with laser illumination show a significant variance in the maximum correlation peaks. The explanation roots in the formation of OLSPs, which are an interference of wavelets from each individual scatterer within the laser spot. This means that even smallest changes of the surface, such as dirt, scratches, or temperature change, can lead to decorrelation of the whole image. As the system is shielded and the scans are conducted in direct sequence, changes of the surface should not be visible at that scale. The more likely explanation is given by the translational decorrelation of OLSPs, as discussed in [15]. As a displacement of a fraction of the size of the laser spot already leads to a change of the OLSP, uncertainties of the reference measurement are directly reflected by a drop of the correlation value.

The second difference is the correlation value for images taken with white light illumination, which always stays at a level of about 0.7 for images at different position. This means that the resemblance between the images is rather high over the entire database, which might be problematic for applications with even longer stroke. Images taken with laser illumination clearly benefit from the randomness of speckle fields, resulting in an extraordinary low correlation value for images at different positions.

The experiment shows that OLSPs exhibit a high sensitivity to position changes and are clearly distinguishable, which is both beneficial for applications with long stroke and possibly high resolution.

### B. Position Accuracy

The position accuracy of both implementations is tested in a second experiment. For generation of the global feature map

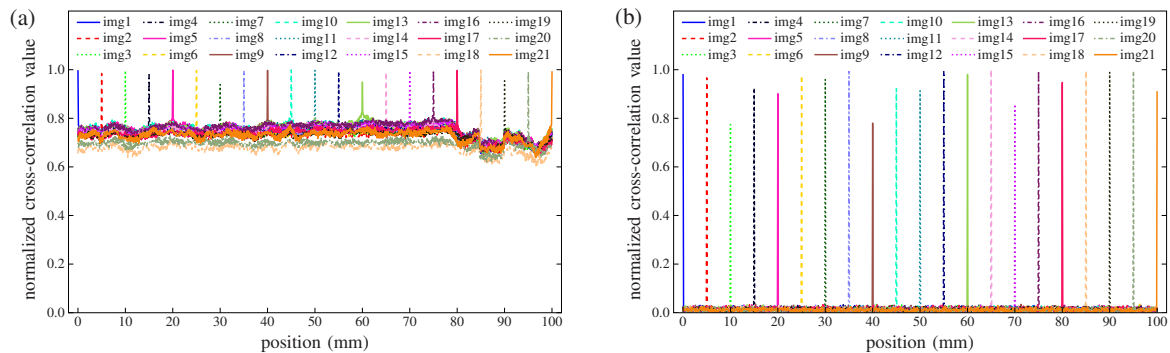


Fig. 7: Resemblance of images taken every 5 mm and the images used for map generation under (a) white light conditions and (b) observation of OLSPs. The random nature of the OLSPs result in a better distinction of individual images, clearly visible by the difference in the normalized cross-correlation value.

the cylindrical rod is scanned with a step size of 1 mm over 100 mm. To ensure independence of the sample set, the scan for the map is executed in an independent scan before the other experiments. The actual coordinates are inferred against the generated feature map using a PF based localization with 100 particles. Fig. 8 shows the absolute position error for both implementations over 10 successive sweeps between 0 mm and 100 mm (trace) and back (retrace) with a step size of 50  $\mu\text{m}$ . The system using white light illumination has a slight positive offset, a peak to peak error of 34.3  $\mu\text{m}$  and an RMS value of 16.6  $\mu\text{m}$ . Under laser illumination the peak to peak error is 22.1  $\mu\text{m}$  and the RMS value is 5.6  $\mu\text{m}$  only. As discussed in [12], in each implementation trace and retrace have strongly correlated position dependent error. This error, which may be caused by the spindle drive (see Section IV-A) or by uncertainties in the map [12], can be used for a calibration of the system for better performance if necessary.

The experiment shows that OLSPs can be used within the framework of the proposed probabilistic sensor. The performance is slightly better than the implementation using white light, although translational decorrelation making features less stable, which can reduce the quality of the stitched map. In addition, the system operates in the micrometer regime even without calibration.

### C. State Recovery

In the last experiment, the state recovery behavior of both implementations is tested, which is required after a sudden power loss. Therefore, the state is assumed to be unknown and initialized by a uniform distribution along the  $x$  coordinate. To ensure a good coverage of the state space during initialization, the particle count is temporarily increased to 5000. To condense the particle cloud to a single hypothesis with small variance, the PF is recursively executed using the actual camera image, but without translation of the target. Theoretically, it would be possible to take the estimate with the strongest weight within the first iteration. Nevertheless, it

proved helpful to follow the described procedure, as it allows to evaluate the evolution of the state convergence by measuring the state uncertainty over all particles. If the state converges quick enough, the actual hypothesis can be taken as center of a new particle cloud with small variance, which also allows to use fewer particles during operation.

The experiment is conducted with different starting position, equally distributed every 5 mm over the whole stroke. The results are summarized in Fig. 9a, showing the estimated position for each run over 40 iterations of the PF, and Fig. 9b showing the according state uncertainty given by the standard deviation.

In the case of while light illumination the state converges within 10 iterations. Nevertheless, state recovery starting from 0 mm failed. This may be a result of the reduced information at the boundaries of the map. This effect is further intensified at the left boundary (0 mm) of the map by the intensity gradient, as described in Section IV.

Under laser illumination, state recovery more frequently failed at the beginning, caused by two or more state hypotheses with similar weight. This is solved by introducing a sample and move strategy at the resampling stage of the PF, which is closely related to regularization described in [25]. This leads to a decreased speed of convergence, but as can be seen from the figures, recovery is achieved from all starting points.

Summarizing, the proposed system is able to measure the absolute position of a cylindrical rod with a peak to peak error of 22.1  $\mu\text{m}$  and an RMS error of 5.6  $\mu\text{m}$  over a measurement range of 100 mm, even if the initial state is unknown. Without the need to modify the measurement target at all, it is as such a promising contactless sensor system for measuring the absolute position on spacious technical surfaces.

## VI. CONCLUSION

This contribution presents a concept of a probabilistic optical absolute position sensor, which can operate on most technical surfaces that might be too smooth for standard

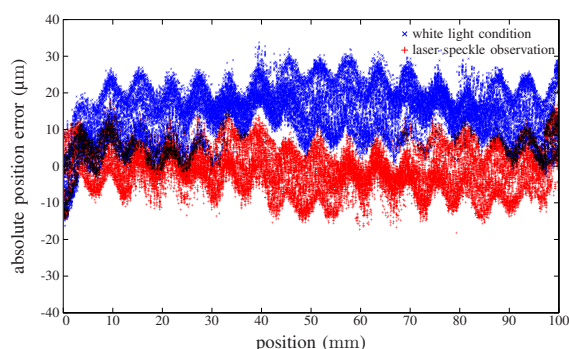


Fig. 8: Absolute position error for the system under white light conditions (blue crosses) and observation of OLSPs (red pluses) over 10 cycles between 0 mm and 100 mm.

camera observation. By means of OLSPs in combination with feature based localization based on a PF, the system is able to estimate the position of a cylindrical rod with a peak error of  $22.1\ \mu\text{m}$  and an RMS error of  $5.6\ \mu\text{m}$  over a measurement range of 100 mm. It is shown that observation of OLSP offers several benefits, such as adjustable but constant average speckle size, a high contrast intensity field, and uniformly distributed features. Further it is shown that the system performance using OLSP is better in comparison to white light illumination in terms of statistical independence, position accuracy, and reliability of state recovery behavior. The statistical independence given by the randomness of the surface enables tracking of the surfaces without additional artificial markers and further allows to extend the measurement range without modification of the algorithms. The resolution is already on the order of several micrometers, but can be easily further improved by implementing an additional calibration step after map generation as already demonstrated in [12]. The initialization scheme presented for state recovery, as necessary after sudden power loss, works well for all measurement positions. A specific strength of the presented approach is the low memory footprint of the generated map, which is about 169 times smaller for white light illumination and 56 for observation of OLSPs in contrast to an implementation based on an image database.

#### REFERENCES

- [1] J. G. Webster and H. Eren, *Measurement, Instrumentation, and Sensors Handbook: Spatial, Mechanical, Thermal, and Radiation Measurement*. Boca Raton, FL, USA: CRC press, 2014, vol. 1.
- [2] F. Seco, J. M. Martín, and A. R. Jiménez, "Improving the accuracy of magnetostrictive linear position sensors," *IEEE Trans. Instrum. Meas.*, vol. 58, no. 3, pp. 722–729, Mar. 2009.
- [3] B. Aschenbrenner and B. Zagar, "Analysis and validation of a planar high-frequency contactless absolute inductive position sensor," *IEEE Trans. Instrum. Meas.*, vol. 64, no. 3, pp. 768–775, Mar. 2015.
- [4] J.-A. Kim, J. W. Kim, C.-S. Kang, J. Jin, and T. Bong Eom, "An optical absolute position measurement method using a phase-encoded single track binary code," *Rev. Sci. Instrum.*, vol. 83, no. 11, p. 115115, 2012.
- [5] H. Wang, J. Wang, B. Chen, P. Xiao, X. Chen, N. Cai, and B. W.-K. Ling, "Absolute optical imaging position encoder," *Measurement*, vol. 67, pp. 42–50, 2015.
- [6] B. Pan, K. Qian, H. Xie, and A. Asundi, "Two-dimensional digital image correlation for in-plane displacement and strain measurement: a review," *Meas. Sci. Technol.*, vol. 20, no. 6, p. 062001, 2009.
- [7] W. Huang, C. Ma, and Y. Chen, "Displacement measurement with nanoscale resolution using a coded micro-mark and digital image correlation," *Opt. Eng.*, vol. 53, no. 12, p. 124103, 2014.
- [8] S. Patzelt, K. Pils, A. Tausendfreund, and G. Goch, "Optical absolute position measurement on rough and unprepared technical surfaces," in *EUSPEN Proc. 12th Int. Conf.*, vol. 1, Jun. 2012, pp. 84–87.
- [9] J. W. Goodman and R. L. Haupt, *Statistical optics*, 2nd ed. John Wiley & Sons, May 2015.
- [10] M. Farsad, G. Goch, and C. Evans, "Displacement measurement using speckle correlation with reduced number of database patterns," in *ASPE Proc. 28th Annual Meeting*, 2013.
- [11] M. Farsad, C. Evans, and F. Farahi, "Robust sub-micrometer displacement measurement using dual wavelength speckle correlation," *Opt. Express*, vol. 23, no. 11, pp. 14960–14972, Jun 2015.
- [12] R. Paris, M. Melik-Merkumians, and G. Schitter, "Vision-based probabilistic absolute position sensor," in *Proc. IEEE Int. Instrum. Meas. Technol. Conf. (I2MTC)*, Pisa, Italy, May 2015, pp. 2066–2071.
- [13] K. A. Stetson, "Vulnerability of speckle photography to lens aberrations," *J. Opt. Soc. Am.*, vol. 67, no. 11, pp. 1587–1590, 1977.
- [14] S. C. Schneider, S. J. Rupitsch, and B. G. Zagar, "Signal processing for laser-speckle strain-measurement techniques," *IEEE Trans. Instrum. Meas.*, vol. 56, no. 6, pp. 2681–2687, 2007.
- [15] R. Paris, T. Thurner, and G. Schitter, "Compensation based displacement measurement using objective laser speckles," in *IFAC 6th Symp. Mech. Sys.*, Hangzhou, China, Apr. 2013, pp. 264–270.
- [16] T. Thurner and C. Zechner, "Phase-based algorithm for 2d displacement estimation of laser speckle patterns," in *Proc. IEEE Int. Instrum. Meas. Technol. Conf. (I2MTC)*. IEEE, 2008, pp. 2173–2178.
- [17] F. Bonin-Font, A. Ortiz, and G. Oliver, "Visual navigation for mobile robots: A survey," *J. Intell. Robot Syst.*, vol. 53, no. 3, pp. 263–296, 2008.
- [18] S. Thrun, W. Burgard, and D. Fox, *Probabilistic Robotics*. MIT Press, 2005.
- [19] R. E. Kalman, "A new approach to linear filtering and prediction problems," *J. Basic Eng.*, vol. 82, no. 1, pp. 35–45, 1960.
- [20] M. Muja and D. G. Lowe, "Fast approximate nearest neighbors with automatic algorithm configuration," in *Int. Conf. Comp. Vis. Theor. Appl (VISSAPP)*, 2009, pp. 331–340.
- [21] P. C. Mahalanobis, "On the generalized distance in statistics," *Proc. National Inst. Sci. Calcutta*, vol. 2, pp. 49–55, 1936.
- [22] R. Szeliski, *Computer vision: algorithms and applications*. Springer Science & Business Media, 2010.
- [23] K. Mikolajczyk and C. Schmid, "Scale & affine invariant interest point detectors," *Int. J. Comput. Vision*, vol. 60, no. 1, pp. 63–86, 2004.
- [24] D. G. Lowe, "Distinctive image features from scale-invariant keypoints," *Int. J. Comput. Vision*, vol. 60, no. 2, pp. 91–110, 2004.
- [25] C. Musso, N. Oudjane, and F. Le Gland, "Improving regularised particle filters," in *Sequential Monte Carlo methods in practice*. Springer, 2001, pp. 247–271.

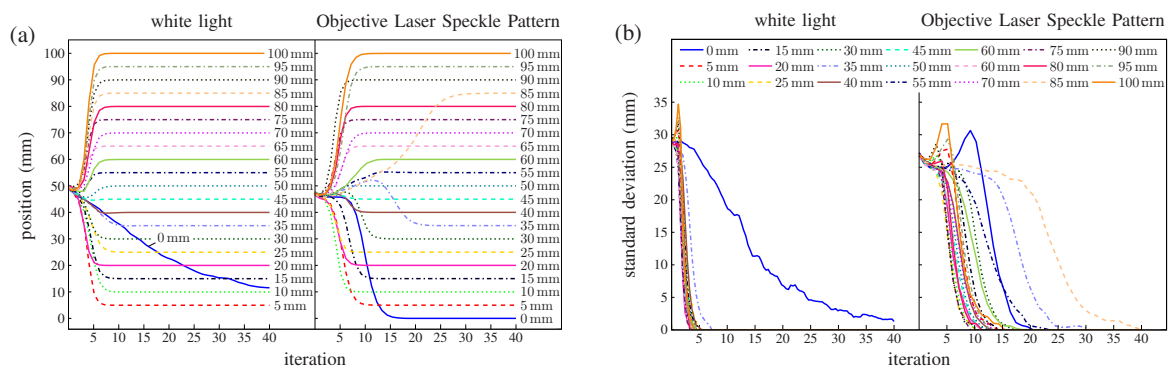


Fig. 9: Comparison of the state recovery behavior of the two tested implementations with (a) showing the position estimates of the PF with different starting positions and (b) the standard deviation of the particles at the same time which allows to evaluate convergence of the state hypothesis.



**Rene Paris** received his master degree in automation at the Vienna University of Technology in 2010. In addition to his studies, he worked from 2008 to 2010 within the field of image processing and automation. Since October 2010, he is research assistant and performs research towards his PhD at the Automation and Control Institute (ACIN), Vienna University of Technology, where his research interests are focused on optical metrology and smart camera based measurement systems.



**Martin Melik-Merkumians** received his master diploma in Electrical Engineering with focus on Industrial Automation at Vienna University of Technology in 2009, and started immediately afterwards a doctoral program at the ACIN within the group for Industrial Automation. His research topics are component-based automation, service-oriented methods and self-learning algorithms in automation systems, as well as knowledge-based development methods for industrial automation software.



**Georg Schitter** is Professor for Industrial Automation at the Automation and Control Institute (ACIN) in the School of Electrical Engineering and Information Technology of the Vienna University of Technology. His primary research interests are on high-performance mechatronic systems and multidisciplinary systems integration, particularly for precision engineering applications in the high-tech industry, scientific instrumentation, and mechatronic imaging systems requiring precise positioning combined with high bandwidths, such as scanning probe microscopy, adaptive optics, and lithography systems for semiconductor industry.